ELSEVIER

Tectonophysics 236 (1994) 179–200

TECTONOPHYSICS

Crustal structure beneath the Kenya Rift from axial profile data

J. Mechie [a,1], G.R. Keller [b], C. Prodehl [a], S. Gaciri [c], L.W. Braile [d], W.D. Mooney [e], D. Gajewski [f,2], K.-J. Sandmeier [a]

[a] *Geophysikalisches Institut, Universität Karlsruhe, Hertzstrasse 16, D-76187 Karlsruhe, Germany*
[b] *Department of Geological Sciences, University of Texas at El Paso, El Paso, TX 79968, USA*
[c] *Department of Geology, University of Nairobi, P.O. Box 14576, Nairobi, Kenya*
[d] *Department of Geosciences, Purdue University, West Lafayette, IN 47907, USA*
[e] *U.S. Geological Survey, Office of Earthquake Research, MS 977, 345 Middlefield Road, Menlo Park, CA 94025, USA*
[f] *Institut für Geophysik, Universität Clausthal, Arnold-Sommerfeld-Strasse 1, D-3392 Clausthal-Zellerfeld, Germany*

Received 27 May 1992; accepted 1 February 1993

Abstract

Modelling of the KRISP 90 axial line data shows that major crustal thinning occurs along the axis of the Kenya Rift from Moho depths of 35 km in the south beneath the Kenya Dome in the vicinity of Lake Naivasha to 20 km in the north beneath Lake Turkana. Low P_n velocities of 7.5–7.7 km/s are found beneath the whole of the axial line. The results indicate that crustal extension increases to the north and that the low P_n velocities are probably caused by magma (partial melt) rising from below and being trapped in the uppermost kilometres of the mantle.

Along the axial line, the rift infill consisting of volcanics and a minor amount of sediments varies in thickness from zero where Precambrian crystalline basement highs occur to 5–6 km beneath the lakes Turkana and Naivasha. Analysis of the P_g phase shows that the upper crystalline crust has velocities of 6.1–6.3 km/s. Bearing in mind the Cainozoic volcanism associated with the rift, these velocities most probably represent Precambrian basement intruded by small amounts of igneous material. The boundary between the upper and lower crusts occurs at about 10 km depth beneath the northern part of the rift and 15 km depth beneath the southern part of the rift. The upper part of the lower crust has velocities of 6.4–6.5 km/s. The basal crustal layer which varies in thickness from a maximum of 2 km in the north to around 9 km in the south has a velocity of about 6.8 km/s.

---

1. Introduction and geology

One of the major aims of the Kenya Rift International Seismic Project (KRISP) 1990 effort was to study the variation in crustal and uppermost mantle structure along the axis of the Kenya Rift. The goal was to detect differences in evolution along the rift axis and to provide a window into the mantle beneath the rift. This paper concentrates on the interpretation of the crustal and P_n phases while an accompanying paper (Keller et al., 1994) concentrates on the interpretation of the deeper mantle phases.

The reconnaissance experiment in 1968 (Griffiths et al., 1971; Griffiths, 1972) and the 1985 preliminary experiment (KRISP Working Group,

---

[1] Present address: GeoForschungsZentrum, Telegrafenberg A3, D-14407 Potsdam, Germany.

[2] Present address: Institut für Geophysik, Universität Hamburg, Bundesstr. 55, D-20146 Hamburg, Germany.

SSDI 0040-1951(94)00030-D

1987; Henry et al., 1990) had already indicated that there might be significant differences in crustal structure between the northern and southern parts of the rift. Although an important pioneering effort, the 1968 experiment was very crude by modern standards with a maximum of only 12 seismograms being recorded over a distance of 350 km and thus reliable phase correlations could not be made between lakes Turkana and Bogoria (Fig. 1). The 1985 KRISP effort produced a preliminary crustal model for the rift south of Lake Baringo, but the lower crustal and upper mantle

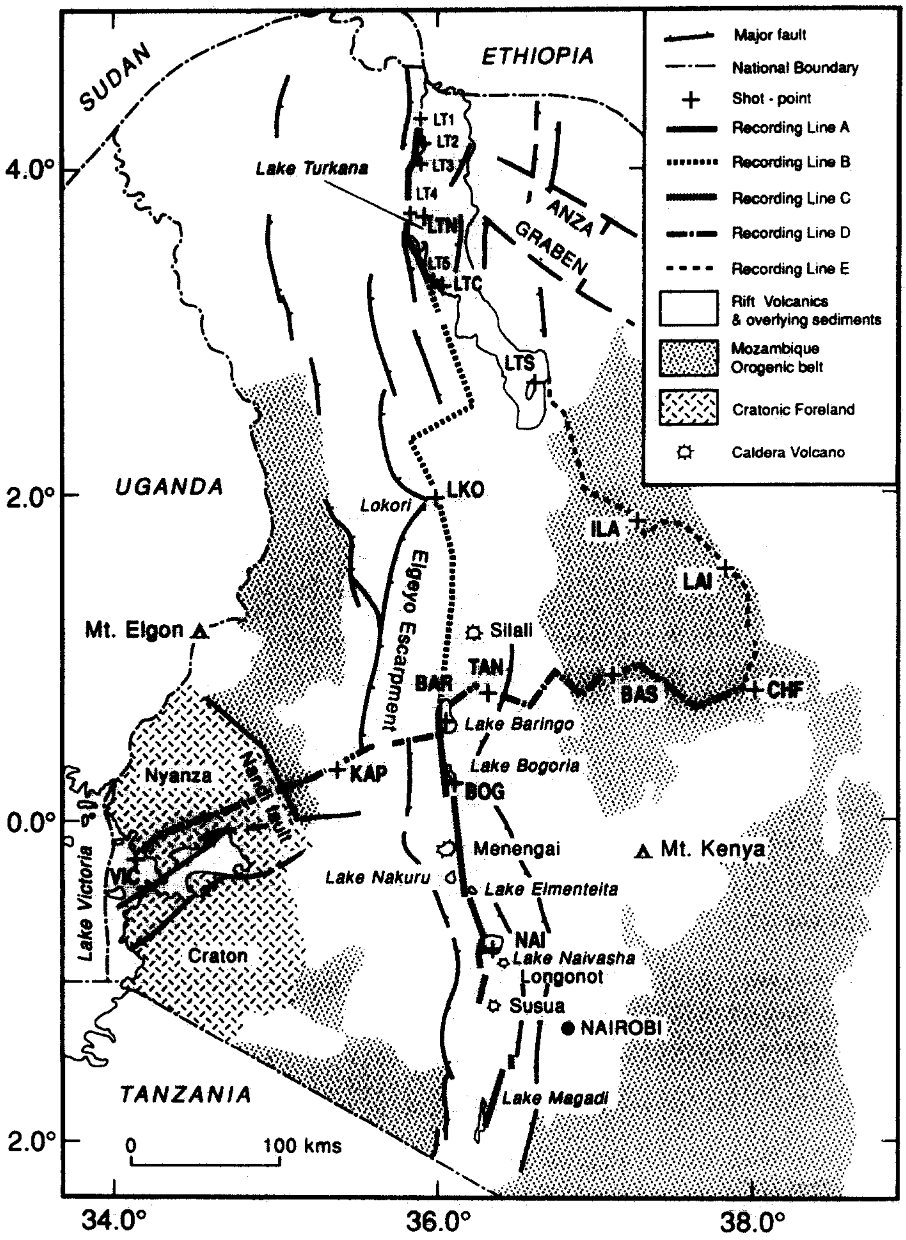

Fig. 1. KRISP 90 location map.

phases were not reversed. Thus these efforts provided a good foundation for the 1990 experiment but left many questions unanswered.

In order to accomplish the above mentioned aims a 600-km-long axial line was completed between lakes Turkana and Magadi in two deployments, B and C (Fig. 1). In deployment B, shots were fired at Lake Turkana North (LTN), Lake Turkana Central (LTC), Lokori (LKO), Lake Baringo (BAR), Lake Bogoria (BOG) and Lake Naivasha (NAI) and the 206 recording stations were set out at 1.5-km intervals between lakes Turkana and Baringo. In deployment C, shots were fired at LTN, LTC, BAR, BOG (2 shots 500 m apart) and NAI and the recording stations were set out at 1–2-km intervals between lakes Baringo and Magadi with a 40-km gap around the volcano Susua. For a more technical description of the experiment the reader is referred to Prodehl et al. (1994b).

The line crosses a variety of geological units ranging in age from Holocene to Precambrian (Fig. 2). The tectonic evolution of that part of the northern Kenya Rift crossed by the seismic line has been described by Morley et al. (1992). The structure and stratigraphy of various areas of the southern portion of the Kenya Rift have been described in detail by Chapman et al. (1978) for the Lake Baringo area, Baker et al. (1988) for the area between Lake Nakuru and Susua (Fig. 1) and Baker and Mitchell (1976) for the area between Susua and Lake Magadi. The northern end of deployment B starts in the Lake Turkana basin in which Plio–Pleistocene and Holocene sedi-

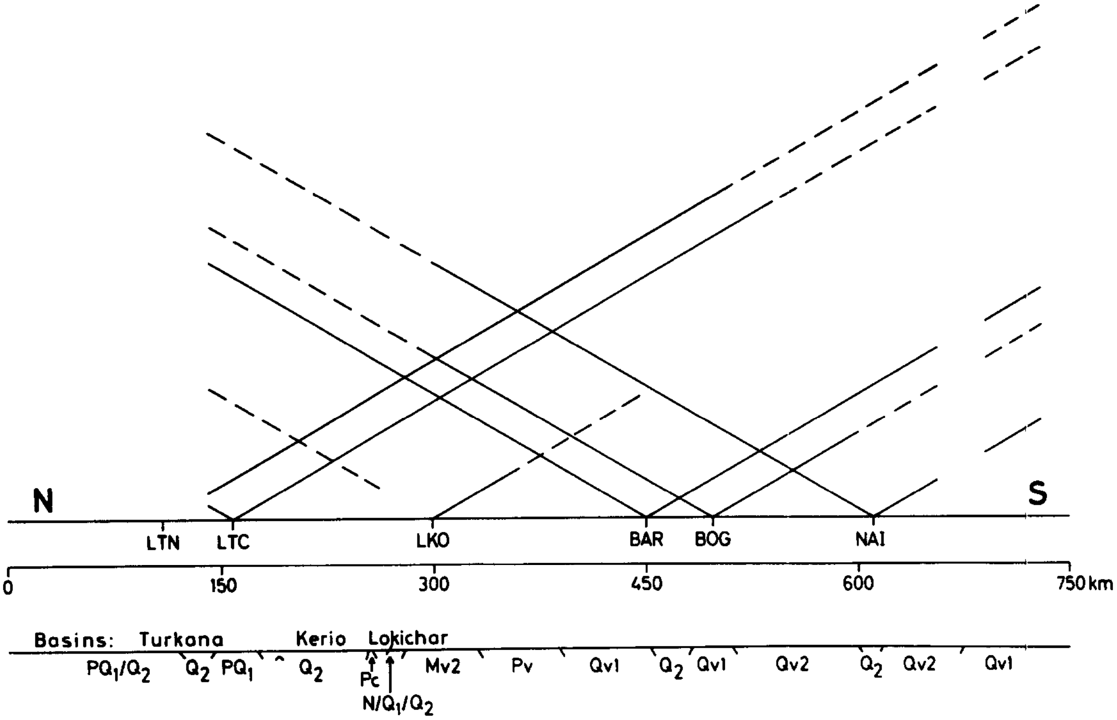

Fig. 2. Geological cross-section drawn from map of Ministry of Energy and Regional Development of Kenya (1987) and observation scheme showing the distribution of shot-points and recording stations. Dashed lines = data recorded but not good; full lines = good data recorded. Key for geological cross-section: *Pc* = Precambrian basement; *N* = Neogene sediments (undifferentiated); *Mv2* = Upper Miocene volcanics; *Pv* = Pliocene volcanics; PQ_1 = Plio–Pleistocene sediments; *Qv1* = Pleistocene volcanics; Q_1 = Pleistocene sediments; *Qv2* = Holocene volcanics; Q_2 = Holocene sediments.

ments are exposed. At about model km 190 it crosses into the Kerio basin in which Holocene sediments are exposed. The line crosses a major fault at model km 253 at the western edge of the Kerio basin. West of this fault the line crosses a steeply tilted block in which Precambrian crystalline basement is exposed. At model km 256 the Precambrian disappears beneath Neogene and Quaternary sediments at the eastern margin of the Lokichar basin. The line leaves the Neogene and Quaternary sediments of the Lokichar basin at model km 280 and crosses onto Upper Miocene volcanics. At model km 330 the line crosses onto Pliocene volcanics and at model km 388 it crosses onto Pleistocene volcanics. Between model km 453 and model km 482 the line crosses the Holocene sediments of the Baringo basin. At model km 510 the line crosses from Pleistocene volcanics onto Holocene volcanics. Between model km 600 and model km 617 the line crosses the Holocene sediments of the Naivasha basin. Finally, between model km 674 and the southern end of deployment C Pleistocene volcanics are exposed.

2. Data

The observation scheme diagram (Fig. 2) shows that recordings were made from all shot-points

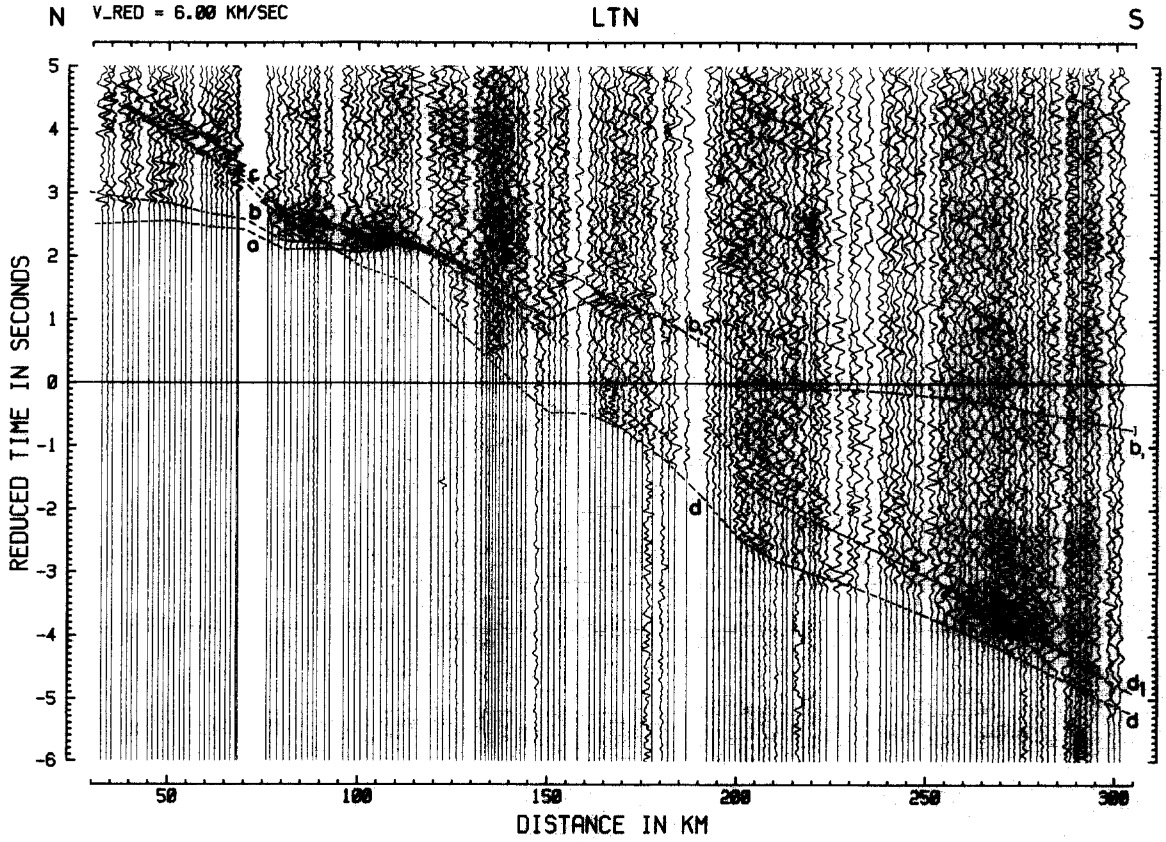

Fig. 3. Trace-normalized low-pass filtered (12 Hz) record section for shot-point LTN recorded to the south along the axial line. Reduction velocity 6 km/s. Phase notation: $a = P_g$, $b_l = P_{i1}P$, $b = P_{i2}P$, $c = P_MP$, $d = P_n$, d_l = upper mantle reflection. Square brackets indicate where b can no longer be seen in the observed data.

except LKO and the northern BOG shot along the whole length of the axial line. Recordings were only made from shot LKO along the northern part of the line, while recordings from the northern BOG shot were only made along the southern part of the line. The observation scheme diagram and the record sections also show that the distance range over which good data were obtained varies from less than 50 km in the case of the LKO-N record section to 300–400 km in the case of the NAI-N, LTC and LTN record sections.

The record sections for LTN and LTC (Figs. 3–6) show clearly the P_g and P_n phases, the first arrival refractions through the upper crystalline crust and the uppermost mantle, respectively. The topography of the base of the rift basins can be well recognized in the travel-time advances and delays of the P_g and P_n phases. Of all the record sections, those from LTN and LTC show the P_MP phase, the reflection from the crust–mantle boundary (Moho), most clearly. Although the intracrustal phase $P_{i1}P$, the reflection from the top of the lower crust, cannot be identified with any certainty on either the LTN or LTC record sections, it can be recognized on the record section for LT4, which is nearby LTN, recorded to the south along line A (Gajewski et al., 1994).

On the LKO-S record section (Fig. 7) only the first arrival direct and refracted phases through the rift infill and the P_g phase can be recognized out to about 60 km distance. This weak shot provided useful control on the basement velocity in this area, although the calculated travel times drawn in for the P_g phase on the record section from the 2-D model are consistently earlier than

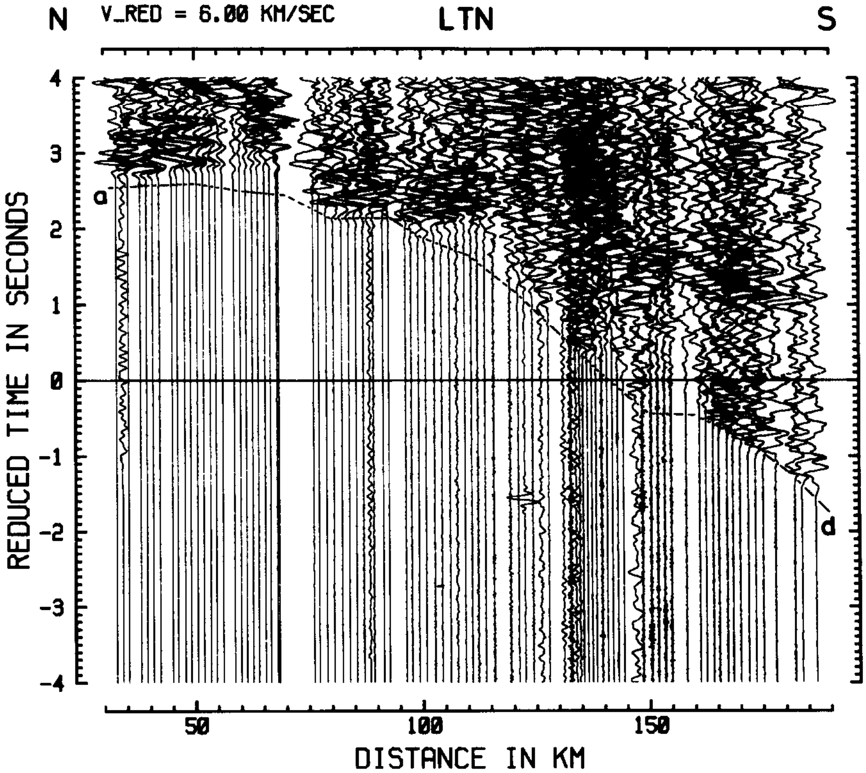

Fig. 4. Trace-normalized low-pass filtered (12 Hz) record section with enlarged amplitudes to show the weak first arrivals for shot-point LTN recorded to the south along the axial line. Reduction velocity 6 km/s. Phase notation: see Fig. 3.

the observed travel times. This travel-time difference may be due to a local delay beneath the shot-point which was located west of the recording line. It was not possible to account for the delay in the 2-D model without degrading the fit to the model significantly for other shot-points.

On the BAR-N and BAR-S record sections (Figs. 8–11), the first-arrival refracted phases through the rift infill can be recognized out to about 15 km distance, after which the P_g phase becomes the first arrival out to about 150 km distance. Beyond about 150 km distance, P_n can sometimes be seen as the first arrival. The $P_{l1}P$ phase can be recognized on both the BAR-N and BAR-S record sections while the intracrustal phase $P_{l2}P$, the reflection from the top of the basal crustal layer, can be recognized on the BAR-S record section. Whereas it is possible to identify the P_MP phase on the BAR-S record section, it is not possible to do so on much of the BAR-N record section.

On the two BOG record sections (Figs. 12, 13), in addition to the first-arrival phases through the rift infill and the P_g phase, the P_n phase can be seen from BOG recorded to the north beyond about 150 km distance (Fig. 13). From BOG recorded to the south both the $P_{l1}P$ and $P_{l2}P$ phases can be seen, while the P_MP phase can be identified in recordings both north and south from BOG.

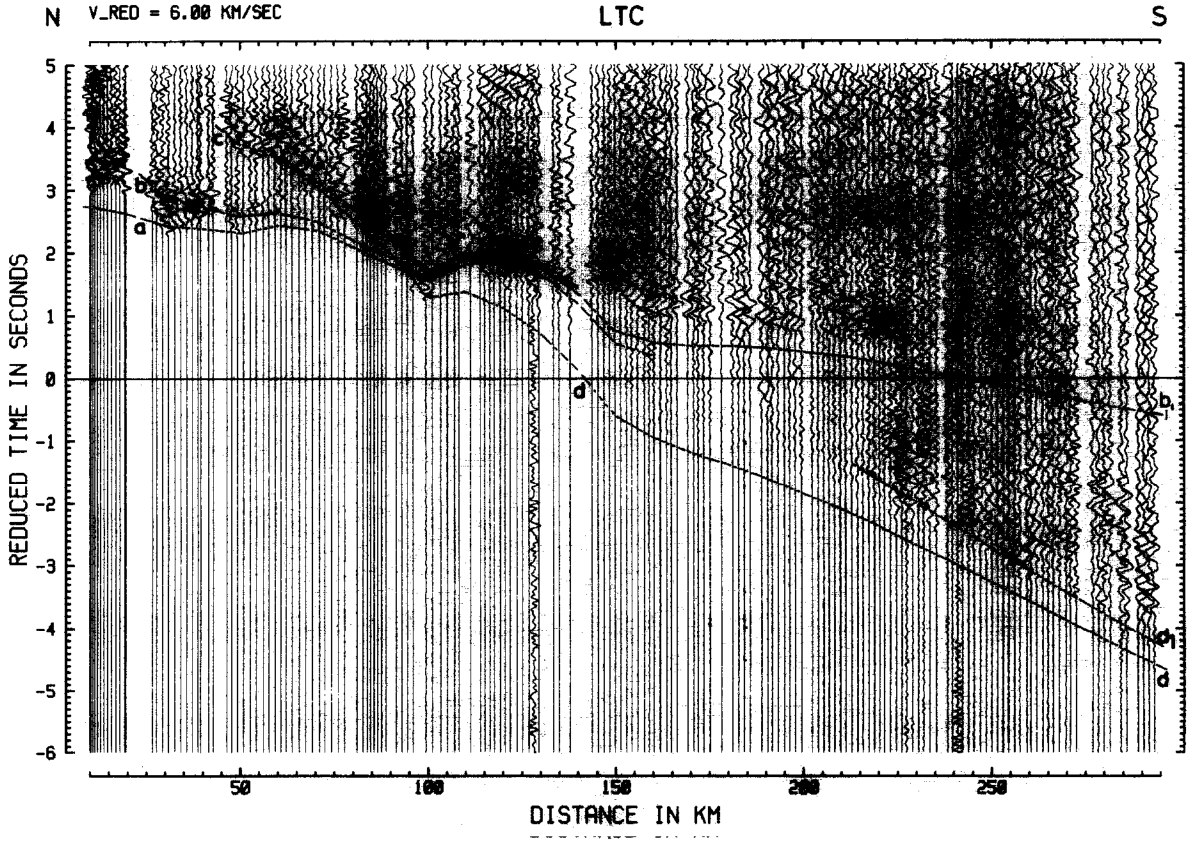

Fig. 5. Trace-normalized low-pass filtered (12 Hz) record section for shot-point LTC recorded to the south along the axial line. Reduction velocity 6 km/s. Phase notation: see Fig. 3. Square brackets indicate where *b* can no longer be seen in the observed data.

On the NAI-N and NAI-S record sections (Figs. 14–16), beyond the first-arrival phases through the rift infill, P_g can be recognized out to about 150 km on the NAI-N record section and out to the end of the NAI-S record section. On the NAI-N record section, beyond about 160 km, P_n occurs as a very weak first arrival in comparison to the crustal phases (Figs. 14, 15). On the NAI-N record section $P_{i1}P$ can be identified. The combined energy of P_MP and P_{i2}, the refracted phase through the basal crustal layer, can be recognized on the NAI-N record section at distances greater than 200 km. The combined energy which is the dominant energy in the record section at distances greater than 200 km is the energy which was taken to be the first arrival in the data recorded northwards from the shot in Lake Bogoria in the 1968 experiment. On the NAI-S record section P_MP can be seen at distances of 100–120 km.

3. Interpretation and model

Interpretation has been carried out mainly using 2-D forward ray-trace modelling (Červený et al., 1977) after preliminary 1-D ray-trace modelling. Synthetic seismograms have been calculated using the ray theoretical technique (Červený et al., 1977), the reflectivity method (Fuchs and Müller, 1971) and, finally, the finite-differences approach. For the finite-differences technique an algorithm for 2-D heterogeneous media by Kelly et al. (1976) with transparent boundary conditions (Reynolds, 1978) and implemented by Sandmeier (1990) was used. The 2-D ray-trace model for the

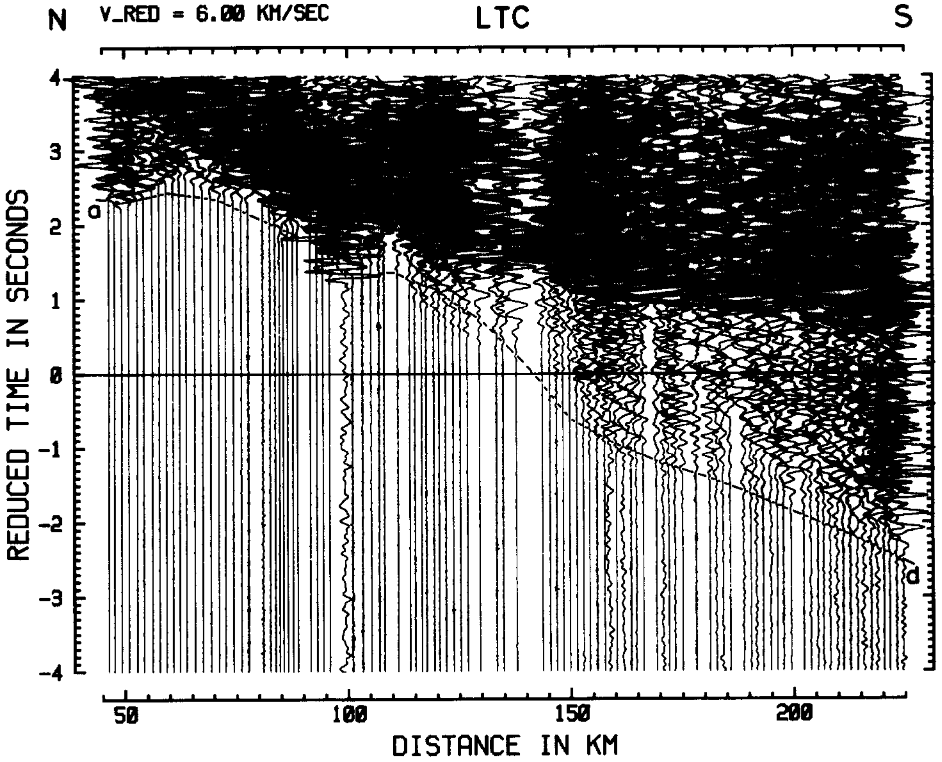

Fig. 6. Trace-normalized low-pass filtered (12 Hz) record section with enlarged amplitudes to show the weak first arrivals for shot-point LTC recorded to the south along the axial line. Reduction velocity 6 km/s. Phase notation: see Fig. 3.

axial line is shown in Fig. 17. The theoretical travel times from this model are drawn in on the record sections (Figs. 3–16). Uncertainties in the velocities and depths can be estimated by perturbing the model until significant differences between observed and theoretical travel times occur.

Beneath the northern part of the rift, the rift infill structure has been derived from the present seismic data supplemented by information from surface geology where the structures are large enough, seismic reflection data (Dunkelman et al., 1988, 1989) and gravity data (Swain and Khan, 1977, 1978; Survey of Kenya, 1982). Beneath the northernmost part of the line the rift infill structure has been adopted as much as possible from line A (Gajewski et al., 1994) from which the rift infill structure can be better defined as the close range station coverage is better. Thus the rift infill structures beneath LTN and LTC have been adopted as much as possible from LT4 and LT5, respectively. Beneath the southern part of the rift between lakes Baringo and Magadi the rift infill structure has been made to agree as much as possible with that derived by Henry et al. (1990) because there were extra shot-points in this region during the 1985 preliminary experiment.

Rift infill velocities vary from about 1.9 km/s near the surface to 5.1–5.2 km/s in the deepest layer below Lake Naivasha. Rift infill thickness varies from zero where Precambrian basement is exposed in the tilted fault block between the Kerio and Lokichar basins to 5–6 km in the Turkana basin and beneath Lake Naivasha. As indicated above the advances and delays in the P_g and P_n phases on the LTN and LTC record sections correlate well with the major basin topography as seen in the surface geology, e.g. the structural highs between the Turkana and Kerio basins at around model km 190 and between the Kerio and Lokichar basins at around model km 255.

P_g apparent velocities can generally be measured to within 0.05 km/s and true velocities to within 0.1 km/s. P_g apparent velocities on the LTN and LTC record sections are disturbed by the severe rift infill topography. Nevertheless, from the line A and the LTN and LTC P_g data, the top of the upper crystalline crust has a velocity of about 6.1 km/s with a small gradient with depth so that a velocity of about 6.15 km/s is reached at 10 km depth. Although a P_g apparent velocity of about 6.0 km/s has been measured on the LKO record section, a high P_g apparent velocity of 6.6–6.7 km/s has been measured on the BAR-N record section between 70 and 150 km distance. Thus the top of the upper crystalline crust between model kms 300 and 400 has a velocity of about 6.3 km/s. Between lakes Baringo and Naivasha, P_g apparent velocities slightly above 6.0 km/s are encountered, whereas the P_g appar-

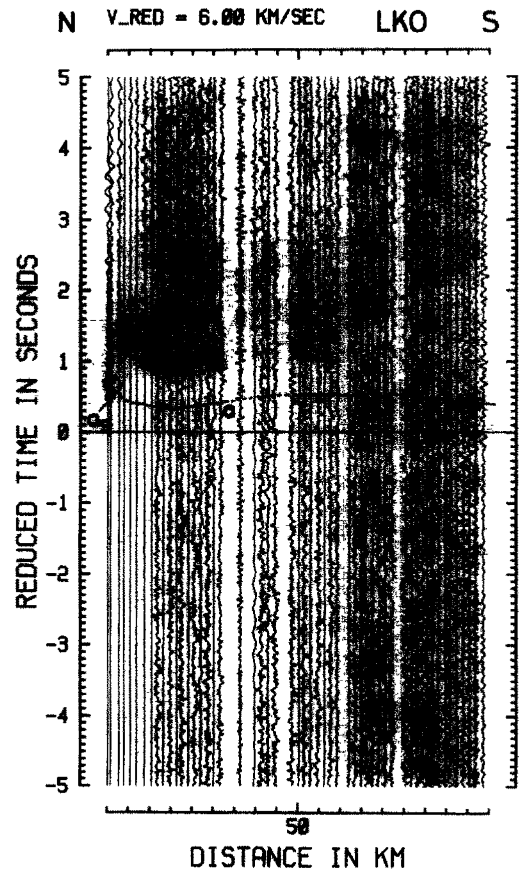

Fig. 7. Trace-normalized low-pass filtered (25 Hz) record section for shot-point LKO recorded to the south along the axial line. Reduction velocity 6 km/s. Phase notation: see Fig. 3 and a_s = direct and refracted phases through rift infill.

ent velocity on the NAI-S record section is about 6.5 km/s due to the shallowing of the basement towards Lake Magadi. Thus, the top of the upper crystalline crust south of Lake Baringo has a velocity of about 6.15 km/s with a small gradient with depth so that a velocity of about 6.25 km/s is reached at a depth of 15 km.

Mainly from analysis of the $P_{i1}P$ reflection, the boundary between the upper and lower crusts beneath the northern part of the rift occurs at about 10 km depth based mainly on the evidence from line A (Gajewski et al., 1994). Beneath the southern part of the rift, the boundary between the upper and lower crusts occurs at about 15 km depth (Fig. 17). Around Lake Bogoria, the only area for which a good estimate is available, the brittle–ductile transition is at about 12 km depth (Young et al., 1991) and thus about 3 km above the boundary between the upper and lower crusts. The velocity at the top of the lower crust has been estimated to be 6.4–6.5 km/s. As no refracted phase has been observed from this layer, the velocity has been estimated mainly from the apparent velocity near the critical point and from amplitude ratios. Thus, the accuracy in the velocity is estimated to be 0.1–0.2 km/s. The accuracy in the depth to the boundary between the upper and lower crusts may be taken to be 1–2 km where observed reflections have originated from this boundary and somewhat greater elsewhere.

The $P_{i2}P$ reflection and the P_{i2} refraction define the presence of the 6.7–6.9 km/s layer. On

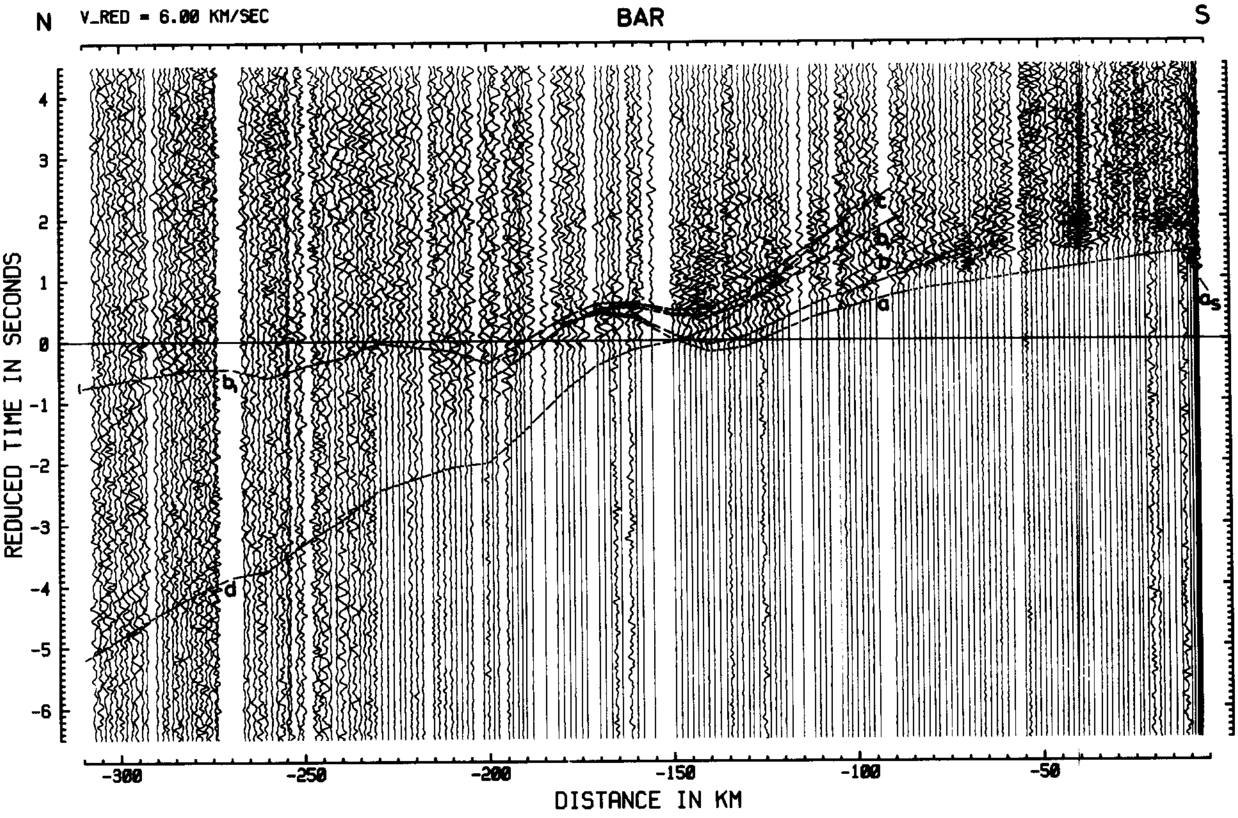

Fig. 8. Trace-normalized low-pass filtered (12 Hz) record section for shot-point BAR recorded to the north along the axial line. Reduction velocity 6 km/s. Phase notation: see Figs. 3 and 7. Square brackets indicate where *b* can no longer be seen in the observed data.

the NAI-N record section the combined P_{i2}, P_MP energy allows an apparent velocity of about 6.8 km/s to be estimated. From $P_{i2}P$ reflections on the BAR-S and BOG-S record sections there appears to be no significant topography on this boundary beneath the southern part of the rift and thus the apparent velocity of about 6.8 km/s on the NAI-N record section must be near the true velocity for this layer. The top of this layer occurs at about 25 km depth beneath the southern part of the rift. In the northern part of the rift there is no evidence on either the LTN or LTC record sections for either the $P_{i2}P$ or P_{i2} phases and the strong crustal reflection at distances greater than 150 km can be better fitted with apparent velocities nearer 6.4–6.5 km/s than 6.7–6.9 km/s. Thus, in the northern part of the rift the 2 km thickness (with which this layer is modelled) is the maximum thickness it can have, otherwise it should have been possible to recognize the $P_{i2}P$ phase at least. In the southern part of the rift the accuracy in the velocity of this layer is estimated to be 0.1–0.2 km/s while the accuracy in the depth to the boundary between the 6.4–6.5 km/s layer and this layer may be taken to be 1–2 km.

On the LTN and LTC record sections the P_MP phase first appears strongly at around 50 km, which should thus be about the critical distance. Although the phase seems to be continuous out to about 200–250 km distance, in the present model P_MP exists only out to about 150 km, beyond which distance the energy is modelled as the reflection $P_{i2}P$ from the top of the 2-km-thick

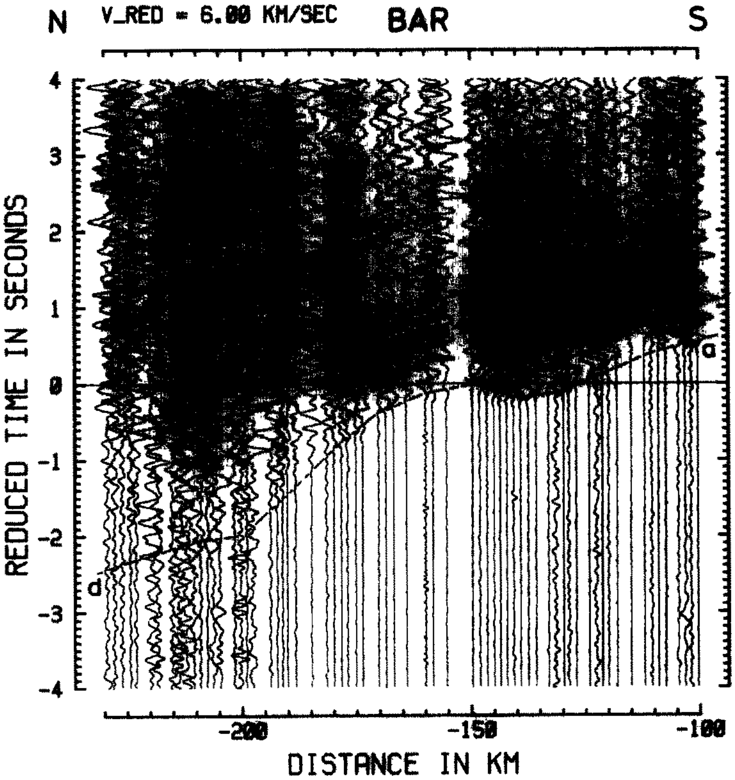

Fig. 9. Trace-normalized low-pass filtered (12 Hz) record section with enlarged amplitudes to show the weak first arrivals for shot-point BAR recorded to the north along the axial line. Reduction velocity 6 km/s. Phase notation: see Fig. 3.

6.7 km/s layer. With a critical distance of about 50 km and a travel-time difference at 50 km of only 1.5 s with respect to the P_g phase and with the P_n phase crossing over the P_g phase to become the first arrival at only 90 km distance, the crust is deduced to be only about 20 km thick beneath the northern part of the rift.

On the BAR-N and NAI-N record sections P_MP arrivals are weak. However, on the BOG-N record section P_MP appears to be stronger. The large distances of about 150 km at which P_n crosses over P_g to become the first arrival on these three record sections indicates that the crust thickens southwards along the rift axis. This is confirmed on the BAR-S, BOG-S and NAI-S record sections by the P_MP phase for which critical distances in excess of 100 km and travel-time differences at 100 km of 2.0–2.5 s with respect to the P_g phase can be seen. It is further confirmed on the BAR-S record section by P_n crossing over P_g to become the first arrival at a distance greater than 150 km. All the evidence shows that the crust beneath the southern part of the rift is about 35 km thick and that the transition from thin crust beneath the northern part of the rift to thick crust beneath the southern part of the rift occurs over a distance of about 150 km between Lokori and Lake Baringo.

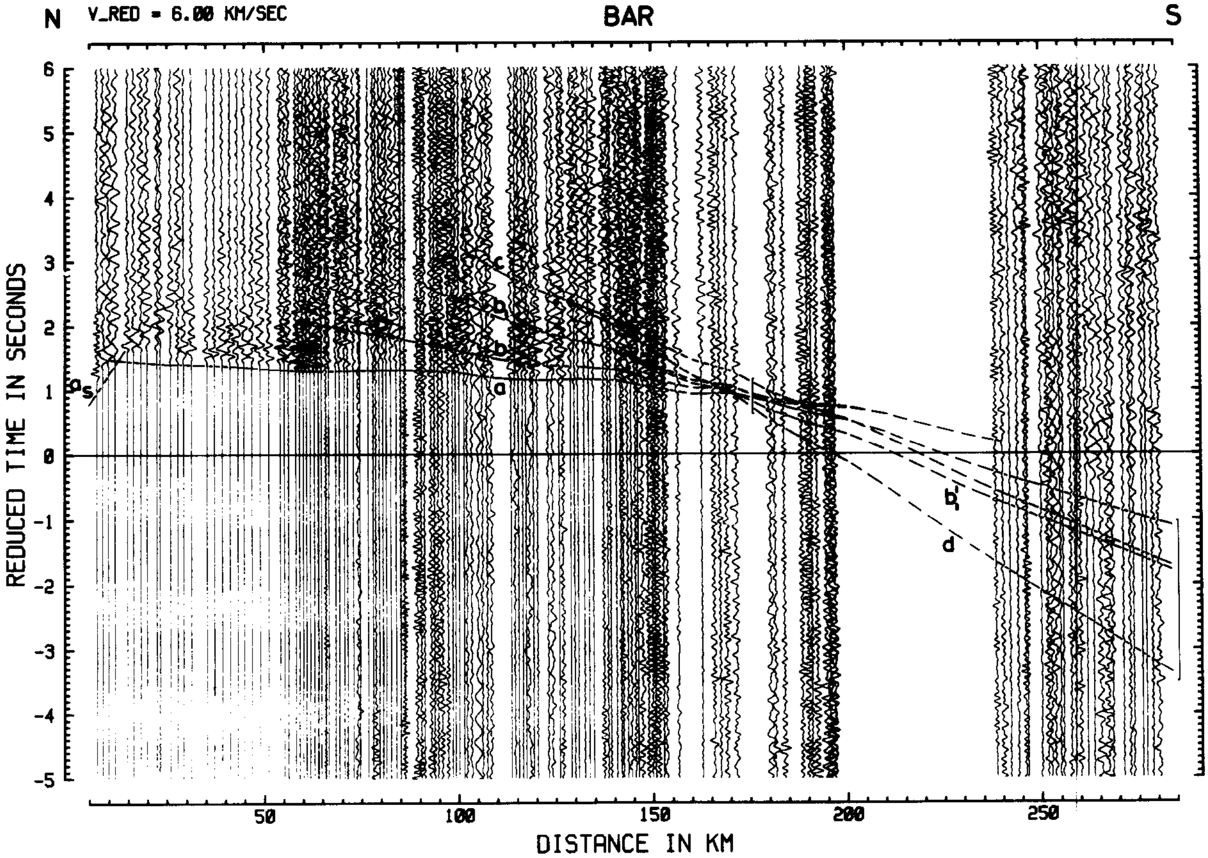

Fig. 10. Trace-normalized low-pass filtered (12 Hz) record section for shot-point BAR recorded to the south along the axial line. Reduction velocity 6 km/s. Phase notation: see Figs. 3 and 7 and $b = P_{i2}$. Square brackets indicate where phases can no longer be seen in the observed data.

From the reversed observations of P_n along the rift axis, the velocity immediately beneath the Moho is calculated to be 7.5–7.7 km/s with a small increase with depth. The accuracy in Moho depths may be taken to be about 2 km.

Ray diagrams and trace-normalized theoretical seismogram sections obtained with the finite-differences approach for the 2-D earth model (Fig. 17) are presented for LTN and BAR-S (Fig. 18). In calculating the finite-differences synthetic seismograms the ray-trace model was digitized at a grid spacing of 40 m which allowed a dominant frequency for the source signal of 2.8 Hz to be utilized. There is general agreement between the observed and theoretical record sections. For example on the LTN record sections, crustal phases dominate out to about 200 km distance beyond which mantle phases are at least as energetic as crustal phases. P_MP is the dominant phase beyond about 50 km distance. On the BAR-S record sections, $P_{11}P$ becomes the dominant phase at about 60 km distance. The $P_{12}P$ phase is not as energetic in the theoretical data as in the observed data. The P_MP phase is dominant beyond about 100 km distance in both sections. The P_n phase is weak compared to later (crustal) phases. One advantage of finite-differences synthetic seismograms is that energy can be obtained at

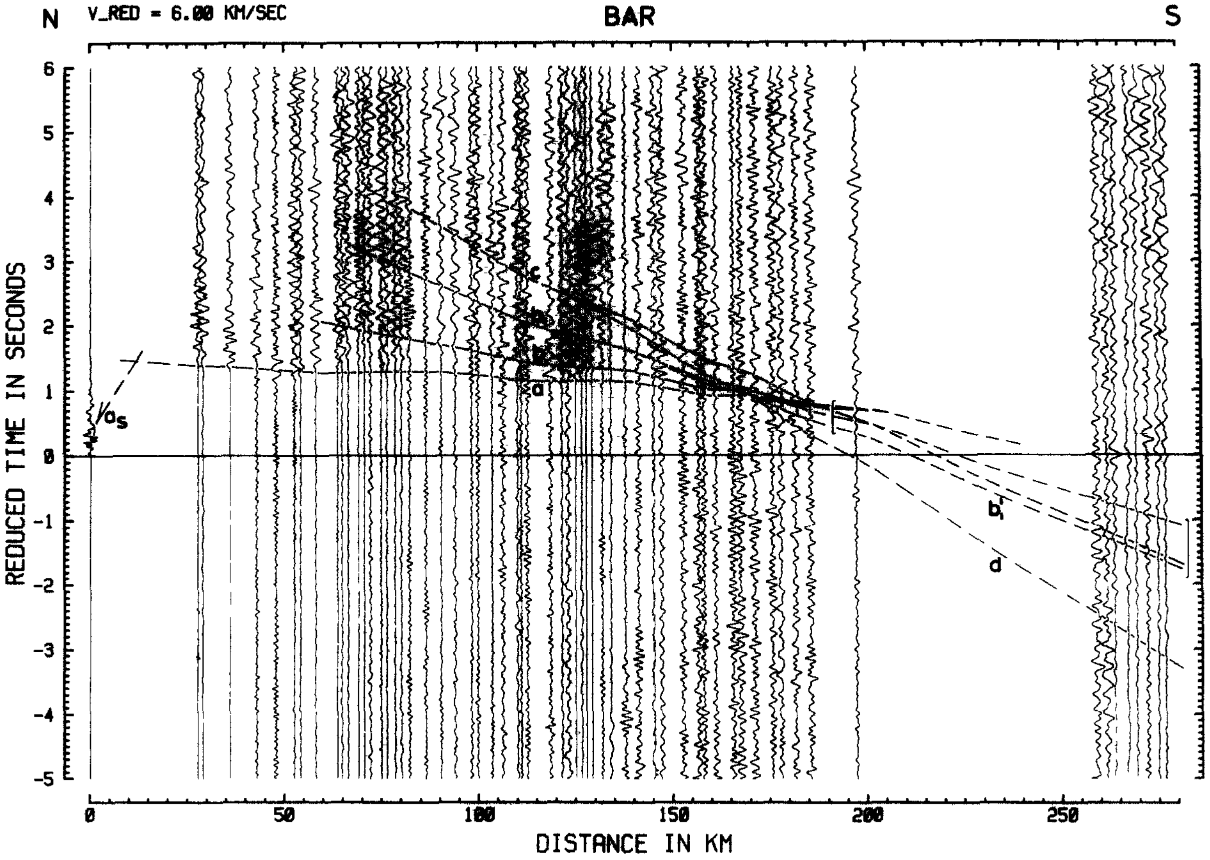

Fig. 11. Trace-normalized low-pass filtered (12 Hz) record section for shot-point BAR recorded to the south along the 1985 axial line. Reduction velocity 6 km/s. Phase notation: see Figs. 3, 7 and 10. Square brackets indicate where phases can no longer be seen in the observed data.

places where ray theory predicts no arrivals. This can be seen, for example, on the ray diagram for LTN in which rays were not found for the P_g and $P_{i1}P$ phases at model kms 249 and 259.

A two and a half dimensional (2.5-D) (Cady, 1980) Bouguer gravity anomaly model compatible with the seismic model is presented for the axial line (Fig. 19). No particular P-wave velocity versus density relationship has been used; only reasonable densities have been assigned to the seismic layers. The most striking feature is that the observed Bouguer gravity anomaly profile (Swain and Khan, 1977, 1978; Survey of Kenya, 1982) can be explained to a first-order approximation by the southwards crustal thickening along the rift axis. Beneath the southern 200 km of the model the densities in the upper crust and the 6.4–6.5 km/s layer of the lower crust have increased by 0.03 g/cm^3. Assuming the Birch Law (Birch, 1961) this is equivalent to a velocity increase of about 0.09 km/s which cannot necessarily be resolved by the seismic model. Some of the small-scale anomalies cannot be adequately explained because some of the gravity stations do not lie close enough to the seismic line and because there are three-dimensional structures present.

4. Discussion and conclusions

Major crustal thinning occurs along the rift axis from Moho depths of 35 km in the south

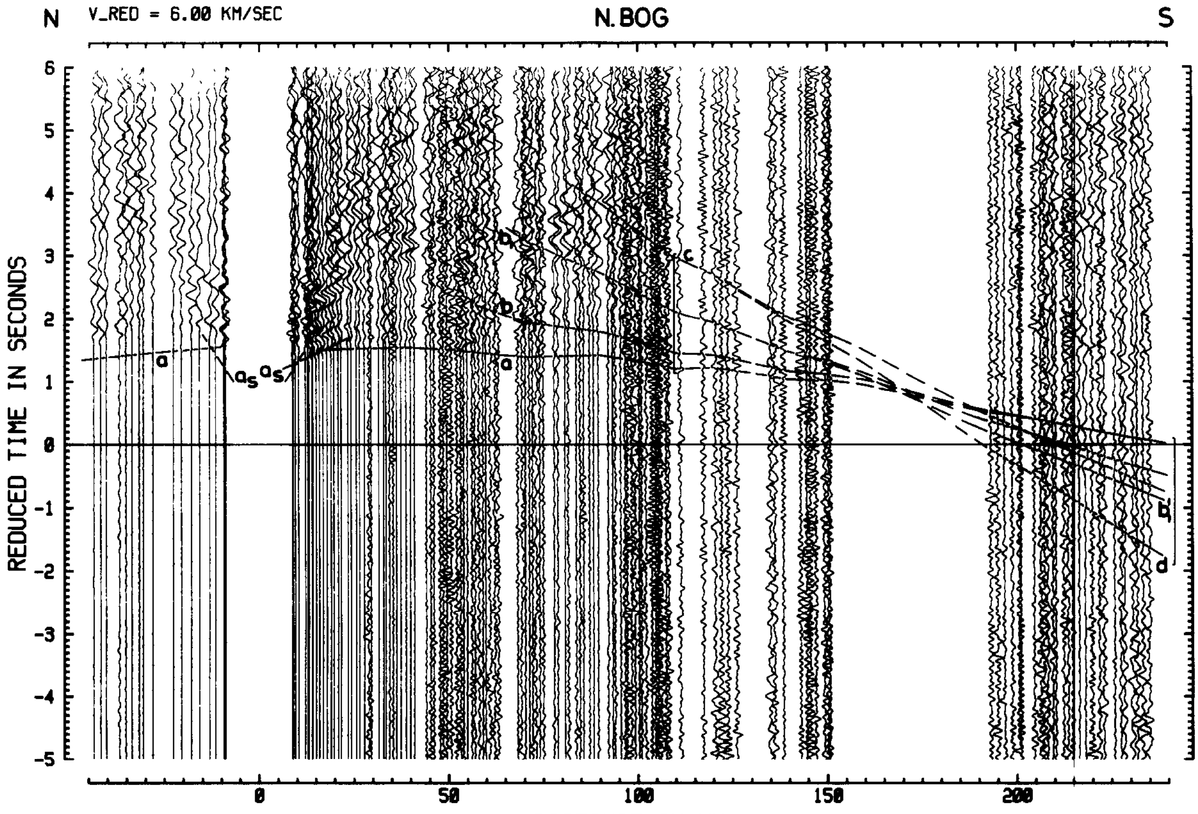

Fig. 12. Trace-normalized low-pass filtered (12 Hz) record section for the northern BOG shot-point recorded along the axial line. Reduction velocity 6 km/s. Phase notation: see Figs. 3, 7 and 10. Square brackets indicate where phases can no longer be seen in the observed data.

beneath the Kenya Dome in the vicinity of Lake Naivasha to 20 km in the north beneath Lake Turkana. Due to the location of the flank line, which lies between the Jurassic Anza graben and the Tertiary Kenya Rift to the south of Lokori, it can be stated that the thinning along the Kenya Rift with respect to that beneath the flank line (KRISP Working Party, 1991; Prodehl et al., 1994a) must have been caused by the Tertiary rifting episode.

Low P_n velocities of 7.5–7.7 km/s are found beneath the whole of the axial line. They seem to be confined more or less to the rift itself as in the vicinity of where the major rift boundaries are crossed, the P_n velocity changes abruptly to 8.0–8.1 km/s (KRISP Working Party, 1991; Maguire et al., 1994).

Crustal velocities beneath the rift itself do not appear to be significantly different to those beneath the flanks (Maguire et al., 1994; Prodehl et al., 1994a) with differences generally less than 0.1 km/s. Thus the expected lowering of seismic velocity due to increased temperature beneath the rift seems to be compensated for by intrusion of mafic material into the crust beneath the rift itself.

The top of the upper crystalline crust has velocities of 6.1–6.2 km/s except between model kms 300 and 400 (Fig. 17), where a velocity of up to 6.3 km/s is encountered. These velocities are

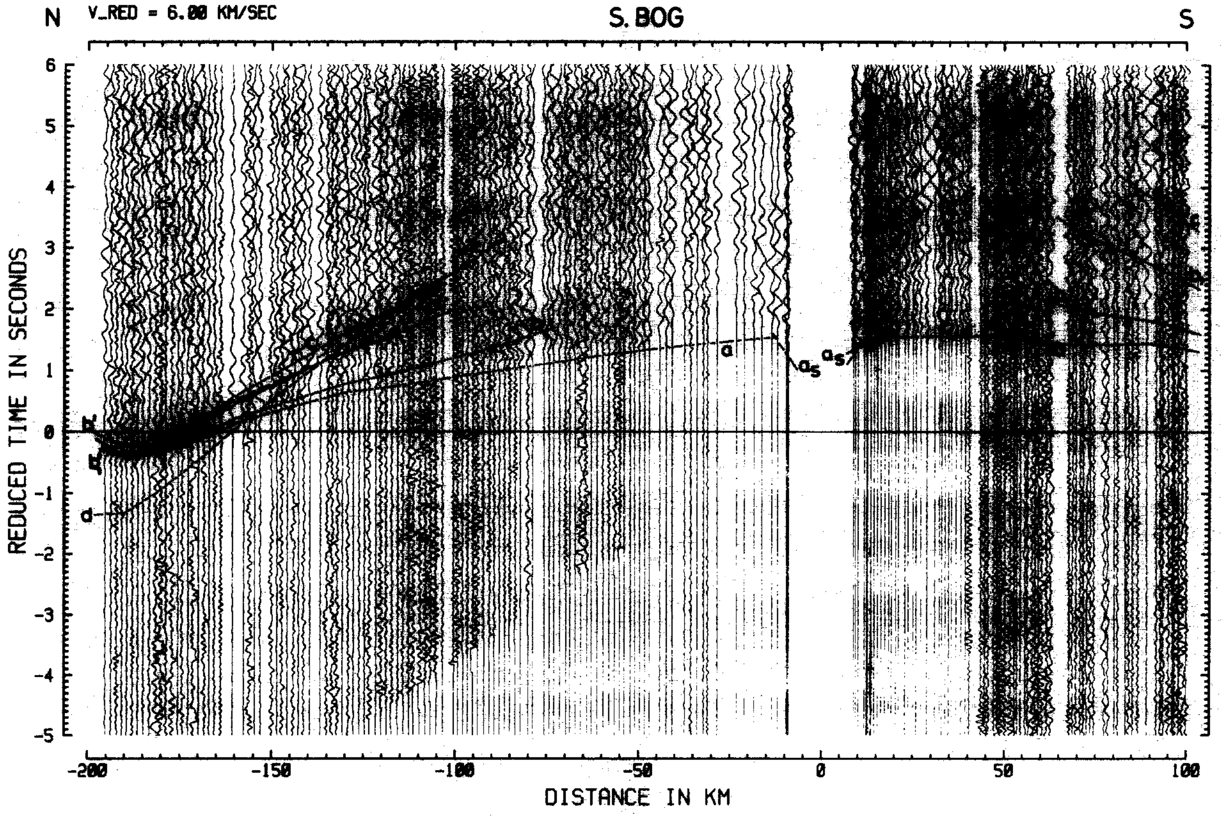

Fig. 13. Trace-normalized low-pass filtered (12 Hz) record section for the southern BOG shot-point recorded along the axial line. Reduction velocity 6 km/s. Phase notation: see Figs. 3, 7 and 10.

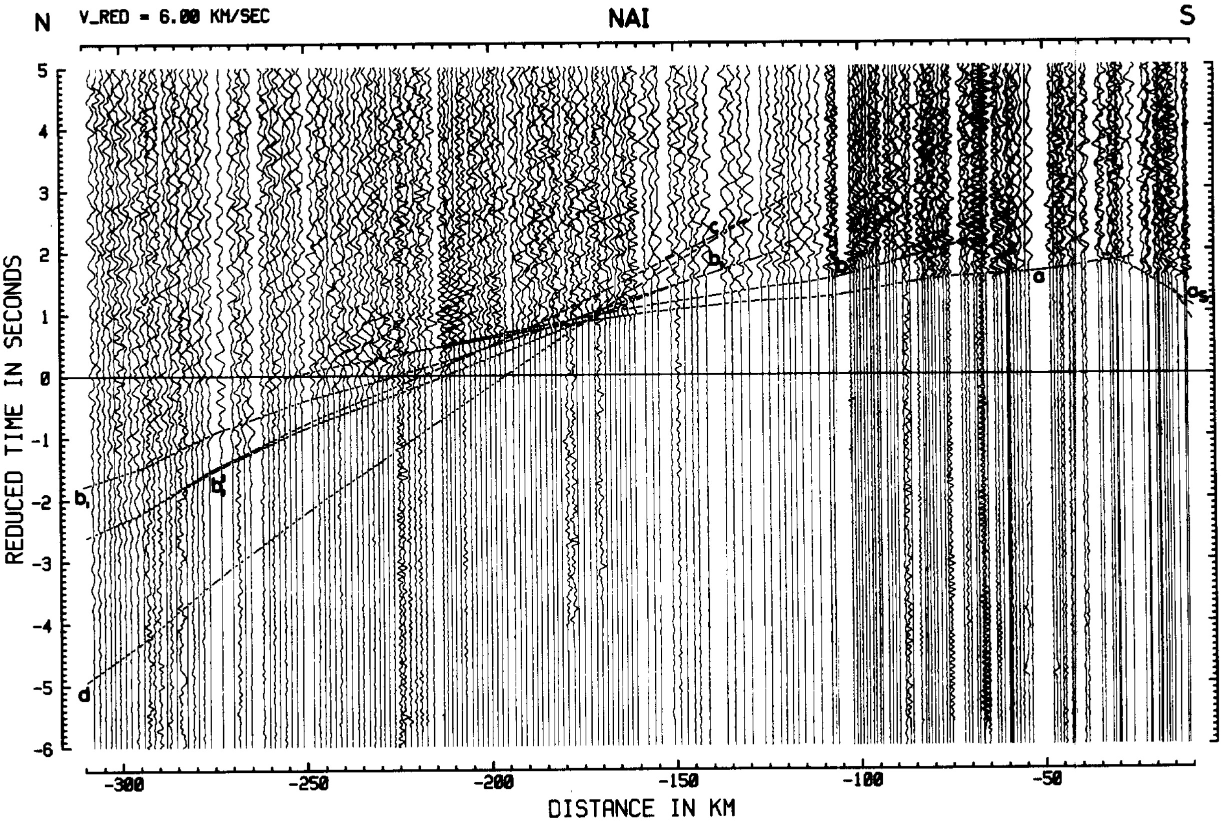

Fig. 14. Trace-normalized low-pass filtered (12 Hz) record section for shot-point NAI recorded to the north along the axial line. Reduction velocity 6 km/s. Phase notation: see Figs. 3, 7 and 10.

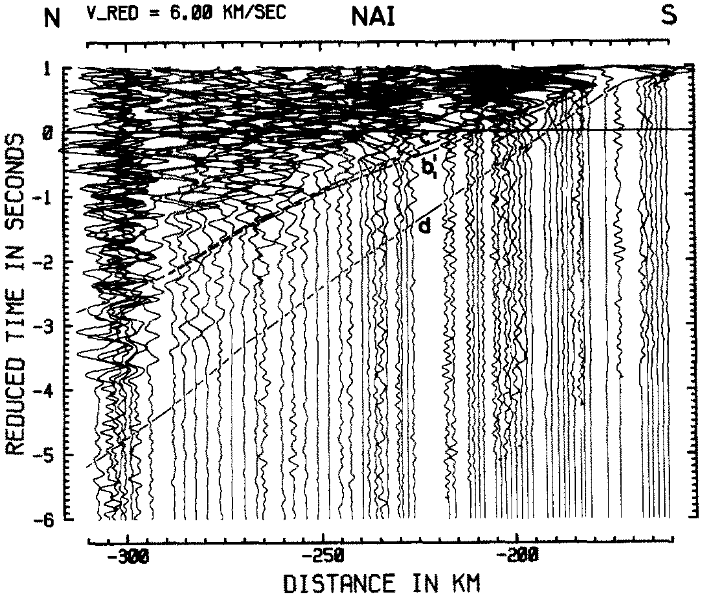

Fig. 15. Trace-normalized low-pass filtered (12 Hz) record section with enlarged amplitudes to show the weak P_n phase for shot-point NAI recorded to the north along the axial line. Reduction velocity 6 km/s. Phase notation: see Figs. 3 and 10.

lower than the estimate of 6.4 km/s which Griffiths et al. (1971) derived for the northern part of the rift between lakes Bogoria and Turkana. They are also lower than the estimate of 6.4–6.6 km/s which Ritter and Achauer (1994) have derived for the area between lakes Baringo and Bogoria. Specifically in this area from the shot-points in lakes Baringo and Bogoria, the data from the seismic line have yielded a reversed velocity determination for the top of the upper crystalline crust of 6.15–6.2 km/s. Beneath the rift flanks where large areas of Precambrian crystalline basement are exposed, the top of the upper crystalline crust has velocities of 5.9–6.2 km/s (KRISP Working Party, 1991; Maguire et al., 1994; Prodehl et al., 1994a). Within the rift itself Precambrian basement is occasionally exposed in structural highs such as that which the seismic line crossed between the Kerio and Lokichar basins (Fig. 17). Thus it seems most reasonable to deduce that the velocities of 6.1–6.3 km/s beneath the rift itself represent Precambrian crystalline basement intruded by small amounts of igneous material, bearing in mind the Cainozoic volcanism associated with the rift. A similar conclusion has been reached by Mooney and Christensen (1994) from a comparison between laboratory measurements on rock samples collected in Kenya and observed seismic velocities.

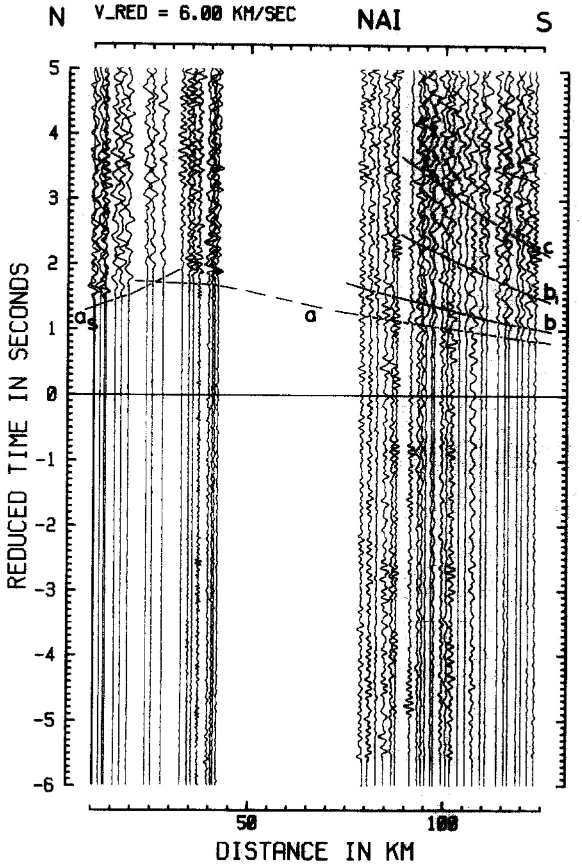

Fig. 16. Trace-normalized low-pass filtered (12 Hz) record section for shot-point NAI recorded to the south along the axial line. Reduction velocity 6 km/s. Phase notation: see Figs. 3, 7 and 10.

The 9-km-thick 6.8 km/s layer beneath the southern portion of the rift can be interpreted in two ways. Firstly, it could be primarily ancient lower crustal material typical of the region (Mozambique orogenic belt). Although typical of lower crustal velocities in stable areas (e.g. Fountain and Christensen, 1989), this velocity is high considering the estimated temperature increase of 300–500°C within the rift at this depth, deduced from the increased geothermal gradient beneath the rift (Morgan, 1983). Thus, the intrusion of more mafic mantle-derived material into the lower crust is required in order to attain the observed velocity. This is the crustal layer that thins most dramatically towards the more extended Lake Turkana region and, considering the geothermal gradient present, ductile flow must be the primary process responsible for this thinning. A second interpretation of the 6.8 km/s lower crustal layer is that it consists mostly of new material added (underplated) to the base of the crust during the rifting process. If allowed to cool for many millions of years, this layer would have velocities in the range 7.0–7.2 km/s. It could then be interpreted to be a "rift pillow" such as has been observed in palaeo-rifts today (e.g. Mooney et al., 1983). If this layer consists predominantly of new material, the difference in the thickness of the pre-rift crust along the rift axis is small.

In the rift itself there is a correlation between crustal thickness, surface topography, Bouguer gravity, thickness of the 6.8 km/s lower crustal layer and rift width. In the south the crust is thick (35 km), surface topography of the Kenya Dome is high (2–3 km), Bouguer gravity is low (down to −220 mGal), the 6.8 km/s lower crustal layer is thick (9 km) and the rift is narrow (50–70 km wide) and well defined. Towards the north, crustal thickness decreases to 20 km beneath Lake Turkana, surface topography decreases to less than 500 m, Bouguer gravity increases to −50 mGal, the 6.8 km/s layer thins dramatically to a maximum of 2 km and the rift widens to 150–200 km. This suggests a northwards change to a highly extended terrain and is compatible with surface estimates of extension of about 10 km in the south (Baker and Wohlenberg, 1971) and 35–40 km in the north (Morley et al., 1992).

The northward increase in extension favours the first of the above explanations for the origin of the 6.8 km/s layer. While underplating can not be totally ruled out, it would appear that ductile stretching is the primary reason for this layer being so thin in the northern portion of the rift. Brittle fracture is surely the dominant process of extension in the upper crust, but the 6.4–6.5 km/s layer is only about 3 km thinner in the north than in the south. It may be supposed that a combination of brittle fracture, ductile flow and magmatic additions to the crust (see e.g. Parsons and Thompson, 1991) is responsible for the present-day crustal structure beneath the rift.

In the upper mantle, combined modelling of the velocity anomalies derived from the teleseismic experiment and the Bouguer gravity leads to the conclusion that a few percent (about 5–6%)

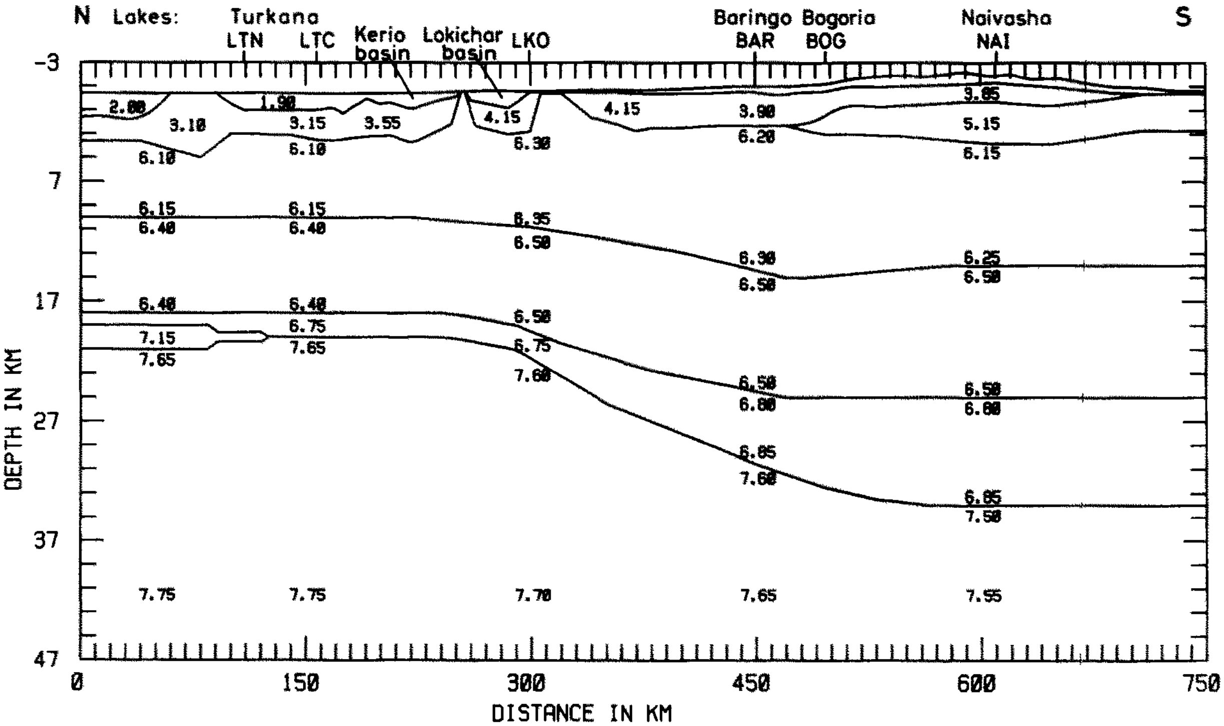

Fig. 17. 2-D ray-trace model for the KRISP 90 complete axial line, including line A. Velocities are accurate to the nearest 0.05 km/s. The layer with average velocity of 7.15 km/s is a transition layer between the 6.7–6.9 km/s layer and the uppermost mantle. The structure north of shot-point LTN has been taken from the interpretation of line A by Gajewski et al. (1994).

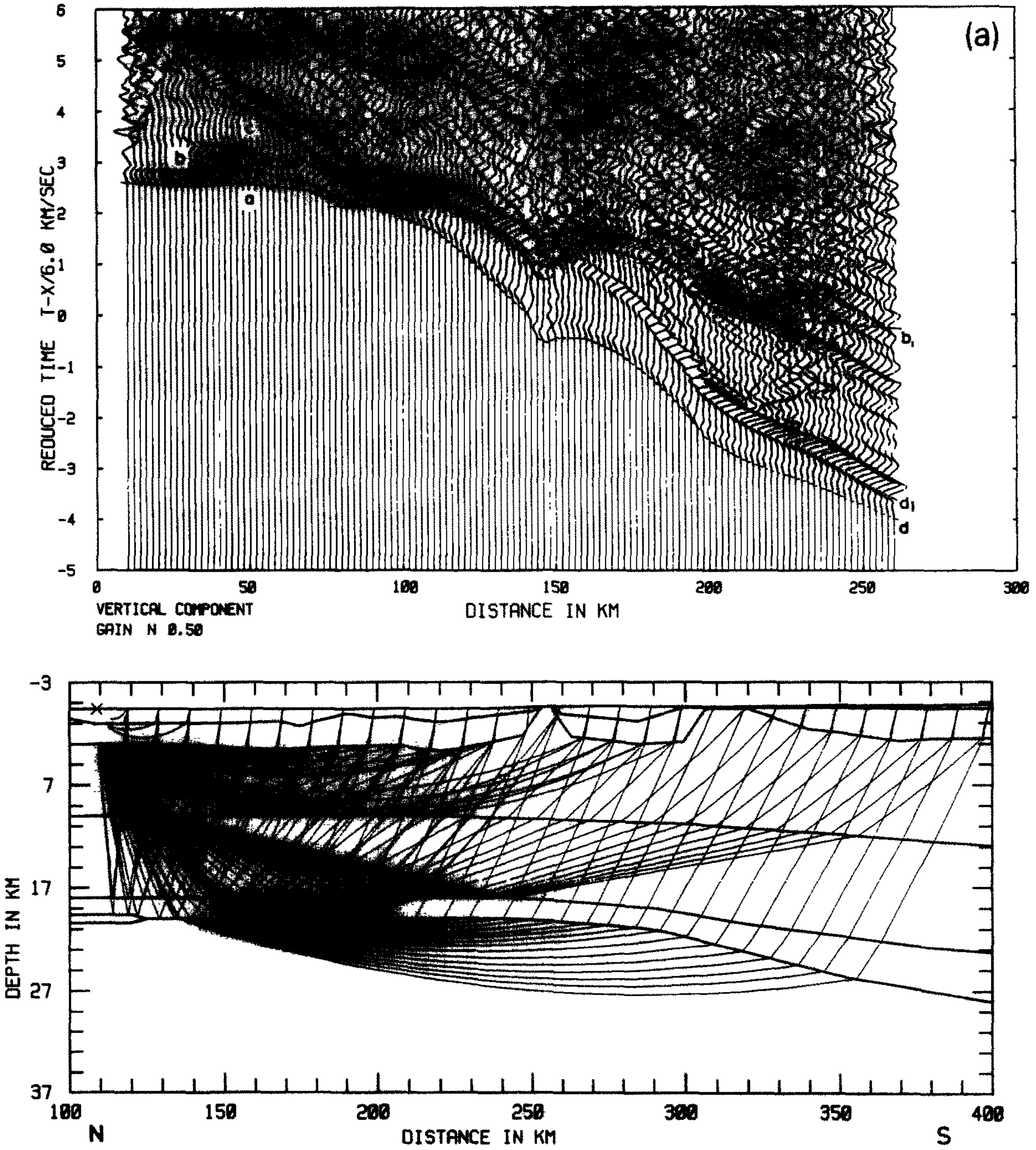

Fig. 18a. Ray diagram and trace-normalized theoretical seismogram section obtained with the finite-differences technique for shot-point LTN recorded to the south. Reduction velocity 6 km/s. Phase notation: see Figs. 3 and 7.

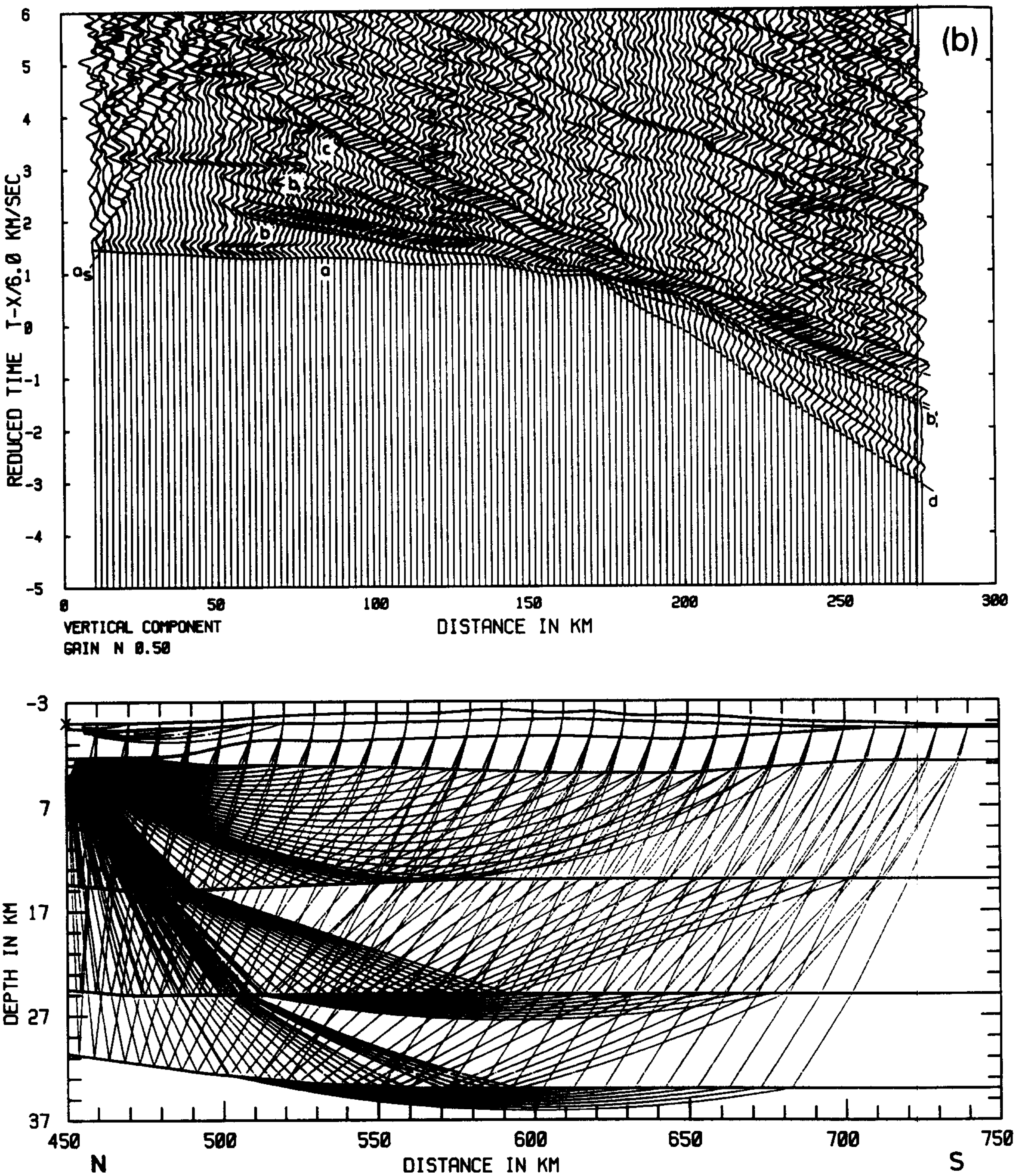

Fig. 18b. Ray diagram and trace-normalized theoretical seismogram section obtained with the finite-differences technique for shot-point BAR recorded to the south. Reduction velocity 6 km/s. Phase notation: see Figs. 3, 7 and 10.

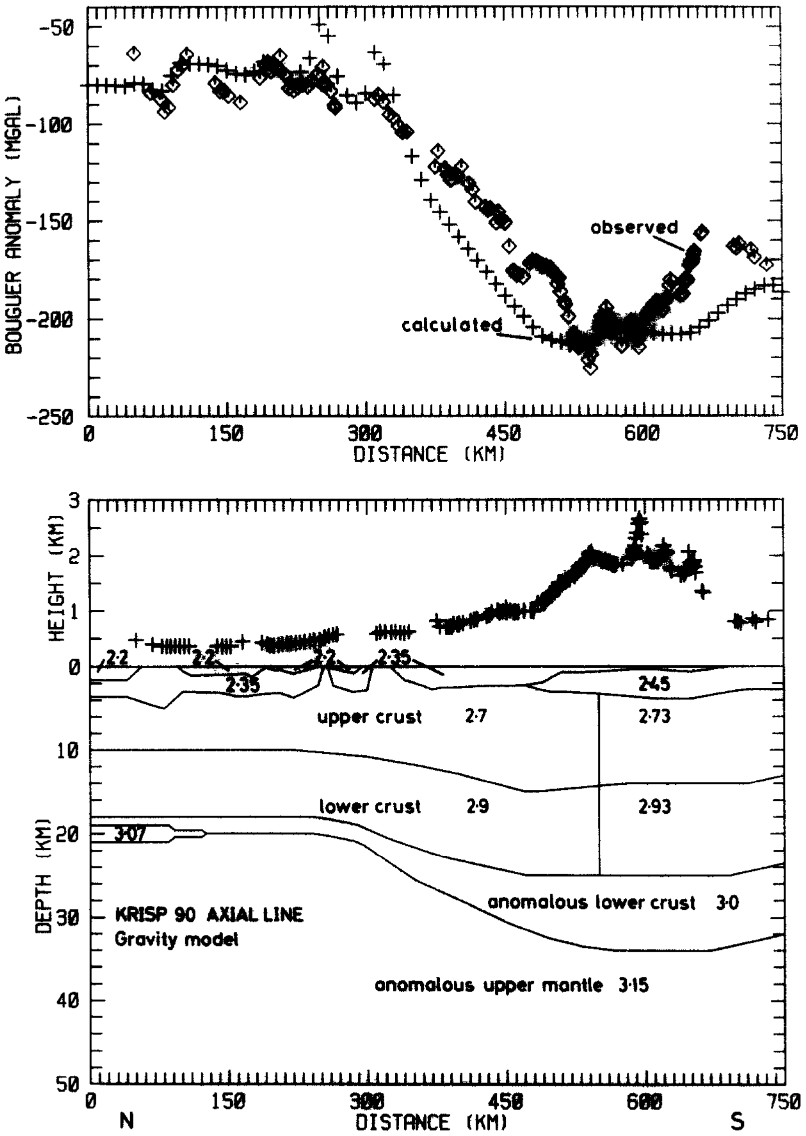

Fig. 19. 2.5-D Bouguer gravity anomaly model compatible with the seismic model for the KRISP 90 axial line. Densities are in g/cm^3.

partial melt is responsible for the low velocities below depths of 40–50 km (Green et al., 1991). In the uppermost kilometres of the mantle (e.g. down to about 40 km depth) the low P_n velocities (down to 7.5 km/s) are probably caused by magma (partial melt) rising from below and being trapped at this level (Mechie et al., 1994).

Acknowledgements

The axial seismic line of the project KRISP 90 was funded by the DFG (Germany) as part of the special research program, SFB 108, "Stress and Stress Release in the Lithosphere" at Karlsruhe University, the NSF (USA), and the EC. The

Kenya Government and many other organizations in Kenya are thanked for making the work possible. The calculations were performed on the Convex C1 supercomputer of the Geophysical Institute at Karlsruhe and the IBM3090 and the Siemens S600 supercomputer of the computer centre at Karlsruhe University. The paper is contribution No. 398 of the SFB 108 and No. 566 of the Geophysical Institute, Karlsruhe University.

References

Baker, B.H. and Mitchell, J.G., 1976. Volcanic stratigraphy and geochronology of the Kedong–Olorgesailie area and the evolution of the South Kenya rift valley. J. Geol. Soc. London, 132: 467–484.

Baker, B.H. and Wohlenberg, J., 1971. Structure and evolution of the Kenya Rift Valley. Nature, 229: 538–542.

Baker, B.H., Mitchell, J.G. and Williams, L.A.J., 1988. Stratigraphy, geochronology and volcano-tectonic evolution of the Kedong–Naivasha–Kinangop region, Gregory Rift Valley, Kenya. J. Geol. Soc. London, 145: 107–116.

Birch, F., 1961. The velocity of compressional waves in rocks to 10 kilobars, part 2. J. Geophys. Res., 66: 2199–2224.

Cady, J.W., 1980. Calculation of gravity and magnetic anomalies of finite-length right polygonal prisms. Geophysics, 45: 1507–1512.

Červený, V., Molotkov, I.A. and Pšenčik, I., 1977. Ray Method in Seismology. University of Karlova, Prague.

Chapman, G.R., Lippard, S.J. and Martyn, J.E., 1978. The stratigraphy and structure of the Kamasia Range, Kenya Rift Valley. J. Geol. Soc. London, 135: 265–281.

Dunkelman, T.J., Karson, J.A. and Rosendahl, B.R., 1988. Structural style of the Turkana rift, Kenya. Geology, 16: 258–261.

Dunkelman, T.J., Rosendahl, B.R. and Karson, J.A., 1989. Structure and stratigraphy of the Turkana rift from seismic reflection data. J. Afr. Earth Sci., 8: 489–510.

Fountain, D.M. and Christensen, N.I., 1989. Composition of the continental crust and upper mantle; a review. Geol. Soc. Am., Mem., 172: 711–742.

Fuchs, K. and Müller, G., 1971. Computations of synthetic seismograms with the reflectivity method and comparison with observations. Geophys. J.R. Astron. Soc., 23: 417–433.

Gajewski, D., Schulte, A., Riaroh, D. and Thybo, H., 1994. Deep seismic sounding in the Turkana depression, northern Kenya rift. In: C. Prodehl, G.R. Keller and M.A. Khan (Editors), Crustal and Upper Mantle Structure of the Kenya Rift. Tectonophysics, 236: 165–178.

Green, W.V., Achauer, U. and Meyer, R.P., 1991. A three-dimensional seismic image of the crust and upper mantle beneath the Kenya rift. Nature, 354: 199–203.

Griffiths, D.H., 1972. Some comments on the results of a seismic refraction experiment in the Kenya rift. In: R.W. Girdler (Editor), East African Rifts. Tectonophysics, 15: 151–156.

Griffiths, D.H., King, R.F., Khan, M.A. and Blundell, D.J., 1971. Seismic refraction line in the Gregory Rift. Nature, 229: 69–71.

Henry, W.J., Mechie, J., Maguire, P.K.H., Khan, M.A., Prodehl, C., Keller, G.R. and Patel, J., 1990. A seismic investigation of the Kenya Rift Valley. Geophys. J. Int., 100: 107–130.

Keller, G.R., Mechie, J., Braile, L.W., Mooney, W.D. and Prodehl, C., 1994. Seismic structure of the uppermost mantle beneath the Kenya rift. In: C. Prodehl, G.R. Keller and M.A. Khan (Editors), Crustal and Upper Mantle Structure of the Kenya Rift. Tectonophysics, 236: 179–199.

Kelly, K.R., Ward, R.W., Treitel, S. and Alford, R.M., 1976. Synthetic seismograms: A finite-difference approach. Geophysics, 41: 2–27.

KRISP Working Group, 1987. Structure of the Kenya rift from seismic refraction. Nature, 325: 239–242.

KRISP Working Party, 1991. Large-scale variation in lithospheric structure along and across the Kenya rift. Nature, 354: 223–227.

Maguire, P.K.H., Swain, C.J., Masotti, R. and Khan, M.A., 1994. A crustal and uppermost mantle cross-sectional model of the Kenya Rift derived from seismic and gravity data. In: C. Prodehl, G.R. Keller and M.A. Khan (Editors), Crustal and Upper Mantle Structure of the Kenya Rift. Tectonophysics, 236: 217–249.

Mechie, J., Fuchs, K. and Altherr, R., 1994. The relationship between seismic velocity, mineral composition and temperature and pressure in the upper mantle—with an application to the Kenya Rift and its eastern flank. In: C. Prodehl, G.R. Keller and M.A. Khan (Editors), Crustal and Upper Mantle Structure of the Kenya Rift. Tectonophysics, 236: 453–464.

Ministry of Energy and Regional Development of Kenya, 1987. 1:1,000,000 Geological Map of Kenya. Nairobi.

Mooney, W.D. and Christensen, N.I., 1994. Composition of the crust beneath the Kenya rift. In: C. Prodehl, G.R. Keller and M.A. Khan (Editors), Crustal and Upper Mantle Structure of the Kenya Rift. Tectonophysics, 236: 391–408.

Mooney, W.D., Andrews, M.C., Ginzburg, A., Peters, D.A. and Hamilton, R.M., 1983. Crustal structure of the northern Mississippi embayment and a comparison with other continental rift zones. Tectonophysics, 94: 327–348.

Morgan, P., 1983. Constraints on rift thermal processes from heat flow and uplift. In: P. Morgan and B.H. Baker (Editors), Processes of Continental Rifting. Tectonophysics, 94: 277–298.

Morley, C.K., Wescott, W.A., Stone, D.M., Harper, R.M., Wigger, S.T. and Karanja, F.M., 1992. Tectonic evolution of the northern Kenya Rift. J. Geol. Soc. London, 149: 333–348.

Parsons, T. and Thompson, G.A., 1991. The role of magma overpressure in suppressing earthquakes and topography: worldwide examples. Science, 253: 1399–1402.

Prodehl, C., Jacob, B., Thybo, H., Dindi, E. and Stangl, R., 1994a. Crustal structure on the northeastern flank of the Kenya rift. In: C. Prodehl, G.R. Keller and M.A. Khan (Editors), Crustal and Upper Mantle Structure of the Kenya Rift. Tectonophysics, 236: 271–290.

Prodehl, C., Mechie, J., Achauer, U., Keller, G.R., Khan, M.A., Mooney, W.D., Gaciri, S.J. and Obel, J.D., 1994b. The KRISP 90 seismic experiment—a technical review. In: C. Prodehl, G.R. Keller and M.A. Khan (Editors), Crustal and Upper Mantle Structure of the Kenya Rift. Tectonophysics, 236: 33–60.

Reynolds, A.C., 1978. Boundary conditions for the numerical solution of wave propagation problems. Geophysics, 43: 1099–1110.

Ritter, J.R.R. and Achauer, U., 1994. Crustal tomography of the central Kenya rift. In: C. Prodehl, G.R. Keller and M.A. Khan (Editors), Crustal and Upper Mantle Structure of the Kenya Rift. Tectonophysics, 236: 291–304.

Sandmeier, K.-J., 1990. Untersuchung der Ausbreitungseigenschaften seismischer Wellen in geschichteten und streuenden Medien. Ph.D. Thesis, Karlsruhe University, Karlsruhe.

Survey of Kenya, 1982. 1:1,000,000 Kenya Bouguer gravity anomaly map. Nairobi.

Swain, C.J. and Khan, M.A., 1977. A Catalogue of Gravity Measurements. Dept. of Geology, Univ. of Leicester, Leicester.

Swain, C.J. and Khan, M.A., 1978. Gravity measurements in Kenya. Geophys. J.R. Astron. Soc., 53: 427–429.

Young, P.A.V., Maguire, P.K.H., Evans, J.R. and Lafolley, N.d'A., 1991. Implications of the distribution of seismicity near lake Bogoria in the Kenya Rift. Geophys. J. Int., 105: 665–674